

Cite this: DOI: 10.1039/c2lc40495h

www.rsc.org/loc

PAPER

# Analysis of pulsed laser plasmon-assisted photothermal heating and bubble generation at the nanoscale†

Edward P. Furlani,<sup>\*ab</sup> Ioannis H. Karamelas<sup>b</sup> and Qian Xie<sup>a</sup>

Received 1st May 2012, Accepted 7th June 2012

DOI: 10.1039/c2lc40495h

A study is presented of photothermal effects associated with nanosecond-pulsed laser-illuminated subwavelength metallic nanoparticles in aqueous solutions. Computational electromagnetic and fluid analysis are used to model fundamental aspects of the photothermal process taking into account energy conversion within the nanoparticle at plasmon resonance, heat transfer to the fluid, homogeneous bubble nucleation, and the dynamic behaviour of the bubble and surrounding fluid. Various nanoparticle geometries are modelled including spheres, nanorods and tori. The analysis demonstrates that the laser intensity and pulse duration can be tuned to achieve controllable bubble generation without exceeding the melting temperature of the particle. The analysis also shows that the particle geometry can be tuned to optimize photothermal energy conversion for bubble generation at wavelengths that span the UV to NIR spectrum. Multiparticle systems are studied and a cooperative heating effect is demonstrated for particles that are within a few radii of each other. This provides more robust bubble generation using substantially reduced laser energy as compared to single-particle systems. The modelling approach is discussed in detail and should be of considerable use in the development of new photothermal applications.

## 1. Introduction

Over the last several years there has been a proliferation of research into the synthesis, characterization and photonic applications of metallic (*e.g.* Au and Ag) nanoparticles.<sup>1–6</sup> This is due in large part to the unique optical properties of such particles, especially manifestations of localized surface plasmon resonance (LSPR). At plasmon resonance, there is a collective and coherent oscillation of free electrons in subwavelength particles that results in an intense absorption and scattering of incident light, as well as highly localized field enhancement. Metallic nanoparticles exhibit this resonance at shape and size-dependent wavelengths that span the ultraviolet (UV) to near-infrared (NIR) spectrum. A desired resonant wavelength can in principle be obtained by controlling the geometry and dimensions of the particles during synthesis. The ability to tune LSPR in this fashion has proven useful for a broad range of applications such as biosensing, optical coherence tomography,<sup>7</sup> photoacoustic imaging,<sup>8</sup> two-photon luminescence imaging,<sup>9</sup> photothermal therapy,<sup>10</sup> photovoltaics and nanoparticle synthesis.<sup>11</sup> In many applications, a femto- or nano-second pulsed laser is used to excite a desired LSPR response of a

nanoparticle.<sup>12</sup> The ability to probe and exploit plasmon-enhanced light-matter interactions occurring in ultra-fast time frames and with nanoscale spatial resolution has spawned fundamental and translational research with broad impact in fields that include analytical and material chemistry, condensed matter physics, nanophotonics and biomedicine.

The plasmonic response of metallic nanoparticles to pulsed laser illumination and the resulting thermal effects in a fluid are of particular interest, especially for bioapplications. These effects depend on many factors including the duration of the laser pulse, the wavelength, polarization and intensity of the incident light, the size and shape of the nanoparticles<sup>13–15</sup> and the physical properties of the fluid. Photothermal energy conversion in laser illuminated metallic nanoparticles in fluid occurs through a succession of processes.<sup>12</sup> At the onset of illumination, free electrons in the nanoparticles absorb energy from the incident photons. The electrons undergo electron-electron scattering and relax to an equilibrium energy distribution within 10–50 fs. These energetic electrons transfer their kinetic energy to the lattice of the nanoparticle through electron-phonon interactions. Thermal equilibrium between the electrons and the lattice occurs on the order of 10 to 50 ps. As the particle (lattice) temperature increases, energy is transferred to the surrounding fluid through phonon-phonon coupling. Initially, there is a discontinuous jump in temperature at the particle-fluid interface due to the mismatch in material properties, but this subsides within a fraction of a nanosecond (100–400 ps).<sup>12</sup> As the particle heats up, thermal energy is transferred to the fluid and a vapour bubble

<sup>a</sup>Department of Electrical Engineering, University at Buffalo, The State University of New York at Buffalo (SUNY-Buffalo), New York, 14260, USA. E-mail: efurlani@buffalo.edu

<sup>b</sup>Department of Chemical and Biological Engineering, University at Buffalo, The State University of New York at Buffalo (SUNY-Buffalo), New York, 14260, USA

† Published as part of a themed issue on optofluidics

will nucleate at the particle-fluid interface if the critical vaporization temperature of the fluid is reached. Once nucleated, a bubble will exhibit a dynamic behaviour (expansion and collapse) that is a complex function of the heat and mass transfer at the bubble-fluid interface as well as the temperature and flow in the surrounding fluid. In this paper, we consider nanosecond-pulsed laser illumination of metallic nanoparticles in fluid leading to bubble nucleation, wherein the pulse duration exceeds the characteristic time constants for the initial non-equilibrium photothermal transients discussed above.

The motivation for this study is to advance fundamental understanding of plasmon-assisted photothermal phenomena and to enable rational design for a growing number of applications. Of particular interest are bioapplications where photothermal nanoparticle-based bubble generation is used for enhanced imaging, drug delivery and localized therapy.<sup>16</sup> With regards to imaging, both metallic nanoparticles and vapour bubbles provide optical contrast within biological tissue, which can be used for refined high-resolution imaging. With regards to therapy, gold nanoparticles can be functionalized to carry therapeutic drugs *in vivo* and to selectively bind to target tissue (*e.g.* cells for uptake). Once in place, the particles can be illuminated to cause localized heating and/or bubble nucleation, which can release surface-bound drug molecules and/or destroy target tissue *via* hyperthermia or structural damage (*e.g.* rupture of cell membrane). Moreover, recent experiments have shown that the photothermal process can be tuned to optimize heating and to control the size and duration of nucleated bubbles.<sup>16</sup> The combined diagnostic and highly localized multimodal therapeutic functionality of plasmon-based photothermal therapy makes it a promising technique for a number of emerging biomedical applications. However, one drawback of this approach is that biological tissue readily absorbs light over an extended portion of the optical spectrum, which can limit the depth of penetration for effective therapy. This can be overcome, to some extent, by tuning the LSPR wavelengths of the nanoparticles to a near-infrared (NIR) biological window of tissue (especially 650–900 nm), which permits deeper penetration on the incident light.

A brief survey of the literature in this field reveals work by several groups.<sup>17–20</sup> Pitsillides *et al.*<sup>18</sup> have used laser-pulsed metallic nanoparticles to cause cellular damage and have demonstrated very selective destruction of target cells with minimal collateral damage to neighbouring cells. Hartland *et al.*<sup>21,22</sup> and Hu and Hartland<sup>23</sup> have characterized fundamental energy dissipation mechanisms in femto-second pulsed laser illuminated Au nanospheres. Volkov *et al.*<sup>24</sup> introduced a one-dimensional hydrodynamic computational model for predicting femtosecond-pulsed laser heating of spherical nanoparticles. Their work suggests that biological damage can be restricted to within a short distance (relative to the particle diameter) from the illuminated particle. Lapotko *et al.*<sup>25–29</sup> have used laser-pulsed gold nanoparticles to create nanobubbles for imaging, diagnosis and therapeutic applications at the cellular level. They have used spherical gold nanoparticles (30 nm diameter) to destroy K562 and human lympholeukemia cells. The nanobubbles generated by these particles ruptured the membranes of target cells, with minimal collateral damage.<sup>28</sup> More recently, Lukianova *et al.*<sup>30,31</sup> have used gold nanoparticles

for effective intracellular drug delivery. Nanoparticles with surface-bound drug molecules were guided to target cells and then the temperature of the nanoparticle-drug carriers was increased using laser pulses. This generated a nanobubble that caused intracellular dispersal of the carried drug, thereby reducing drug dose and treatment time while increasing effectiveness. Despite the recent progress in this field, relatively few theoretical studies have focused on the details of plasmon-assisted bubble nucleation and the subsequent bubble and fluid dynamics considered here.

In this paper we study nanosecond-pulsed, laser-induced, plasmon-assisted bubble generation around subwavelength metallic nanoparticles in aqueous solutions and associated thermal and fluidic effects. We consider gold nanoparticles, but the theory readily applies to other plasmonic materials (*e.g.* Ag). We use continuum theory to model the photothermal process. The continuum analysis involves the combined use of computational electromagnetics to predict photonic effects, and computational fluid dynamics (CFD) to predict coupled thermal-fluid-phase change effects. Various nanoparticle structures are studied, including spheres, rods and tori. We first model each of these geometries in isolation, as single particle systems, as illustrated in Fig. 1. The modelling provides a detailed understanding of the photothermal process, *i.e.* photothermal energy conversion within the particle at its plasmon resonant frequency, temperature rise within the particle, heat transfer from the particle to the fluid, phase change leading to bubble nucleation, and the dynamic behaviour of the bubble and surrounding fluid during and after the pulsed illumination. We also study multiparticle systems and demonstrate that cooperative heating between neighbouring particles gives rise to bubble nucleation at reduced laser intensity.

To the best of our knowledge, this is the first study of pulsed-laser plasmon-assisted nanoscale bubble nucleation using combined computational electromagnetic and CFD-based fluidic analysis. This approach enables fundamental understanding and rational design of pulsed laser nanoparticle-based plasmon-assisted photothermal processes and should prove useful for the development of novel photothermal applications.

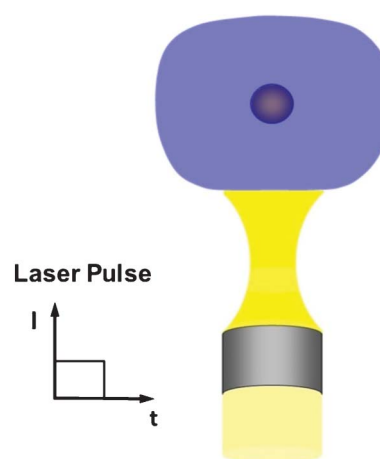


**Fig. 1** Pulsed-laser illumination of a gold nanosphere in fluid.

## 2. Theory and modelling

We study the laser-induced plasmon-assisted photothermal effects using continuum level photonic and fluidic analysis. The photonic analysis is performed using computational electromagnetics and is used to predict photothermal energy conversion within the nanoparticles, *i.e.* the time-averaged power absorbed by a particle as a function of the wavelength, intensity and polarization of the incident light. Maximum power absorption occurs at the plasmon resonance wavelength, which depends on the size, geometry and electrical properties (permittivity) of the particle.<sup>13–15</sup> The absorbed power is converted into heat and thus the particle becomes a heat source within the fluid. The heating of the fluid due to direct absorption of photons is assumed to be negligible in this analysis.

The fluidic analysis is performed using CFD and is used to predict thermal, pressure and flow effects including the temperature rise in the particle, heat transfer from the particle to the fluid, phase change within the fluid leading to homogeneous bubble nucleation, the dynamic behaviour of the bubble as it expands and collapses, and the temperature, pressure and flow throughout the fluid during the entire process. The fluidic analysis is used to determine the threshold power and pulse duration needed to generate and sustain a bubble with a desired dynamic behaviour. Once this is understood, the laser intensity needed to produce the threshold power within the particle is back-calculated from the photonic analysis.

The plasmon-based photothermal process studied here is highly complex. It involves coupled phenomena that span multiple length and time scales, which depend on the duration and power level of the laser pulse. A rigorous analysis of this process would require concurrent multiscale modelling that encompasses quantum to continuum level theory. To the best of our knowledge, no such models have been reported. Previous theoretical studies in this field are based to some extent on simplifying assumptions. In this paper, we make the assumption that the photothermal process can be modelled using continuum theory over the range of variables that we consider.

The continuum approach can be justified based on several factors. First, we consider laser pulse durations of multiple nanoseconds, which is longer than the characteristic time constants of the transient non-equilibrium photothermal effects discussed above, *i.e.* electron–electron scattering (10–50 fs), electron–phonon/lattice interactions (10–50 ps), and phonon–phonon interactions at the surface of the particle ( $\sim 100$ –400 ps).<sup>32</sup> Second, we study the response of metallic nanoparticles with dimensions ( $\sim 60$  nm) that are greater than the phonon mean free path ( $\sim 20$  nm in gold).<sup>33</sup> Therefore, the phonon Knudsen number is  $\sim 0.3$ , which implies that continuum thermal analysis can provide a reasonable estimate of thermal behaviour. Similarly, as shown below, nucleated bubbles have dimensions ( $\sim 60$  nm) that are greater than the mean free path ( $\sim 10$ –15 nm) of the vapour molecules within them. Thus, the Knudsen number for the gas dynamics is  $\sim 0.25$ . Lastly, the fluidic domain is on the order of 200–300 nm, which is suitable for continuum fluid dynamics. Details of the modelling are described in the following paragraphs.

### 2.1 Photonic analysis

The photonic response of metallic nanoparticles in fluid is predicted using three-dimensional (3D) full-wave time-harmonic

field theory. Maxwell's equations are solved assuming a time dependence of the form  $\mathbf{E} = \mathbf{E}(\mathbf{x})e^{i\omega t}$ . We use TEM analysis where the equation for the E-field reduces to

$$\nabla \times (\mu_r^{-1} \nabla \times \mathbf{E}) - k_0^2 \left( \epsilon_r - j \frac{\sigma}{\omega \epsilon_0} \right) \mathbf{E} = 0 \quad (1)$$

where  $\mu_r$  and  $\epsilon_r$  are the relative permeability and permittivity of the media, respectively. For metallic nanoparticles,  $\epsilon_r$  is complex-valued and frequency-dependent. For gold nanoparticles,  $\epsilon_r$  can be represented in closed form,

$$\epsilon_{r,Au}(\lambda) = \epsilon_\infty - \frac{1}{\lambda_p^2 \left( \frac{1}{\lambda^2} - i \frac{1}{\gamma_p \lambda} \right)} + \sum_{n=1,2} \frac{A_n}{\lambda_n} \left[ \frac{e^{i\phi_n}}{\left( \frac{1}{\lambda_n} - \frac{1}{\lambda} + i \frac{1}{\gamma_n} \right)} + \frac{e^{-i\phi_n}}{\left( \frac{1}{\lambda_n} + \frac{1}{\lambda} - i \frac{1}{\gamma_n} \right)} \right] \quad (2)$$

A description of this expression and the various parameters in it are given in the references.<sup>34–36</sup> It is important to note that eqn (2) is valid for a time-harmonic dependence of the form  $\exp(-i\omega t)$ . However, we use the COMSOL RF program (www.comsol.com) for the photonic analysis, which is based on an  $\exp(i\omega t)$  time-harmonic dependence. Therefore,  $\epsilon_r$  in our analysis is obtained by replacing the imaginary terms in eqn (2) with their complex conjugates (*i.e.* by replacing  $i$  by  $-i$ ). The fluid surrounding the nanoparticle is assumed to be non-absorbing water with an index of refraction of  $n_f = 1.333$ .

For the photonic analysis, we use a rectangular computational domain as shown in Fig. 2a. This domain contains a single spherical nanoparticle located at the origin and is discussed in detail in the analysis of spherical nanoparticles below. Perfectly matched layers (PMLs) are applied at the top and bottom of the domain to reduce backscatter from these boundaries as described in the references.<sup>37,38</sup> Perfect electric conductor (PEC, symmetry) conditions are applied at the boundaries perpendicular to  $\mathbf{E}$ , and perfect magnetic conductor (PMC, symmetry) conditions are applied at the boundaries perpendicular to  $\mathbf{H}$ . These symmetry boundary conditions ensure normal incidence of the respective fields at the boundaries transverse to the direction of propagation. They therefore mimic a 2D array of identical nanoparticles with centre-to-centre  $x$  and  $y$  lattice spacing equal to the width of the computational domain in the  $x$  and  $y$  directions, respectively. These boundary conditions simplify the analysis and the lattice distances are chosen to be large enough so that the resulting predictions will reflect the response of a single particle, *i.e.* negligible coupling with neighbouring particles.

The particle is illuminated with a uniform downward-directed TEM plane wave with  $\mathbf{E}$  parallel to the  $x$ -axis (Fig. 2a). The incident field is generated by a time-harmonic surface current positioned in the  $x$ - $y$  plane directly below the upper PML.<sup>37,38</sup> Throughout this paper, the magnitude of the surface current is chosen to provide a plane wave in the fluid with a peak amplitude of  $E_x = 2 \times 10^6 \text{ V m}^{-1}$  (in the absence of the particle). This choice of field amplitude is arbitrary as we are ultimately interested in the power absorbed by the particle  $Q_{abs}$  (watts) per unit irradiance  $I_{inc}$  (watts/m<sup>2</sup>). The absorbed power, which is wavelength dependent, is converted to heat and thus this analysis

predicts photothermal energy conversion within the particle. The power level in the nanoparticle and corresponding pulse duration that are needed to nucleate and sustain a bubble without damaging the particle are computed using CFD analysis as described below. Once a viable power level is known, the laser irradiance required to generate this power within the nanoparticle is computed from the photonic analysis.

## 2.2 Fluidic analysis

We use CFD to study heat transfer from the particle to the fluid, phase change leading to bubble nucleation, and the bubble-fluid dynamics. The volume of fluid (VOF) method as implemented in the FLOW-3D software (www.flow3d.com) is used for this analysis.<sup>39</sup> The fluid is assumed to be incompressible and Newtonian with surface tension  $\sigma$ , viscosity  $\mu$ , density  $\rho$ , specific heat at constant pressure  $c_p$  and thermal conductivity  $k$ . These are assumed to be constant in our analysis. The equations governing heat and mass transfer are as follows:

**Navier–Stokes:**

$$\rho \left( \frac{\partial \mathbf{v}}{\partial t} + \mathbf{v} \cdot \nabla \mathbf{v} \right) = -\nabla p + \mu \nabla^2 \mathbf{v} \quad (3)$$

**Continuity:**

$$\nabla \cdot \mathbf{v} = 0 \quad (4)$$

**Heat transfer:**

$$\rho c_p \left( \frac{\partial T}{\partial t} + \mathbf{v} \cdot \nabla T \right) = k \nabla^2 T, \quad (\text{fluid}) \quad (5)$$

$$\rho_{np} c_{np} \frac{\partial T_{np}}{\partial t} = Q_{abs}(t) + k_{np} \nabla^2 T_{np}, \quad (\text{nanoparticle}) \quad (6)$$

where  $\mathbf{v}$ ,  $p$  are the velocity and pressure in the fluid and  $\rho_{np}$ ,  $c_{np}$  and  $k_{np}$  are the density, specific heat at constant pressure and thermal conductivity of the nanoparticle, respectively.  $Q_{abs}$  is the power generated uniformly within by the nanoparticle due to absorption of incident laser light,  $T$  and  $T_{np}$  are the corresponding temperatures in the fluid and the nanoparticle. We study the behaviour of gold nanoparticles using the following material properties:  $\rho_{gold} = 19\,300 \text{ kg m}^{-3}$ ,  $c_{gold} = 129 \text{ J kg}^{-1} \text{ K}$  and  $k_{gold} = 317 \text{ W m}^{-1} \text{ K}$ . In all our simulations the gold nanoparticles are immersed in an aqueous solution, which has the properties of water at 300 K. The contact angle for the fluid at the surface of the nanoparticle is assumed to be  $30^\circ$ .

In addition to the physical equations, initial and boundary conditions are imposed to obtain a consistent theory. Heat transfer at the particle-fluid interface is determined using an effective transfer coefficient that takes into account local variations in thermal conduction and convection at this surface. This coefficient can vary along the surface, especially when its shape changes, as in the case of a nanorod. The variation in this coefficient can impact the local formation and growth of a bubble.

## 2.3 Phase change and bubble dynamics

Phase change that initiates bubble nucleation occurs when the fluid reaches its superheat temperature at the surface of the

particle, which is taken to be  $T = 580 \text{ K}$  for  $\text{H}_2\text{O}$ . Before nucleation, the temperature in the particle and surrounding fluid is calculated based on eqns (5) and (6). Heat transfer at the particle–fluid interface is predicted using a local effective transfer coefficient that is dynamically determined. Once a bubble is nucleated, its interface is tracked using the VOF method. The pressure in the bubble is initially set to the saturation pressure at the superheat temperature (approximately 100 Atm), which is computed using the Clausius–Clayperon equation:

$$p_{sat}(T) = p_l \exp \left[ \frac{\Delta H_{vap}}{R} \left( \frac{1}{T_l} - \frac{1}{T} \right) \right] \quad (7)$$

where  $p_l$  and  $T_l$  are the pressure and temperature at a point on the saturation curve (e.g.  $p_l = 100 \text{ kPa}$ ,  $T_l = 273 \text{ K}$ ),  $\Delta H_{vap}$  ( $40.65 \times 10^3 \text{ J mol}^{-1}$ ) is the molar enthalpy of vaporization and  $R$  ( $8.314462 \text{ J mol}^{-1} \text{ K}$ ) is the universal gas constant. This pressure exerts an outward force at the liquid–vapour interface that causes the vapour region to expand into a bubble. As the bubble evolves, the pressure  $p_{vap}$ , temperature  $T_{vap}$  and density  $\rho_{vap}$  of the vapour within it are computed using the equation-of-state of an ideal gas

$$p_{vap} = (\gamma - 1) \rho_{vap} C_{vap,v} T_{vap} \quad (8)$$

where  $c_{vap}$  is the specific heat of the vapour at constant volume and  $\gamma = c_{vap,p}/c_{vap,v}$  is the ratio of specific heats. The pressure, temperature and density are assumed to be spatially uniform (i.e., homogeneous) within the bubble. The mass flux at the fluid–bubble interface is taken to be proportional to the deviation of the fluid from its saturation conditions,

$$\dot{m} = \sqrt{\frac{MW}{2\pi R}} \left( c_{evap} \frac{p_l^{sat}}{\sqrt{T_l}} - c_{cond} \frac{p_{vap}}{\sqrt{T_{vap}}} \right) \quad (9)$$

where  $MW$  is the molecular weight of the vapour,  $R$  the vapour gas constant,  $T$  is temperature in K, and the subscripts  $l$  and  $vap$  refer to liquid and vapour phases, respectively. The term  $p_l$  is the saturation pressure corresponding to the liquid temperature  $T_l$ , and  $c_{evap}$  and  $c_{cond}$  are accommodation coefficients for evaporation and condensation.

After the bubble has nucleated, the nanoparticle is surrounded by vapour and there is negligible heat transfer at the particle–vapour interface. Thus, if the laser pulse continues beyond nucleation, the temperature of the nanoparticle will rise rapidly as it absorbs incident light while being essentially insulated. Under this condition, the nanoparticle can reach its melting or even vaporization temperature within a nanosecond or less. For bulk gold, these values are  $T_m = 1336 \text{ K}$  and  $T_{vap} = 2933 \text{ K}$ , respectively. However, experiments have shown that Au nanoparticles have a lower melting point that can differ by as much as 200 K from the bulk value. Specifically, the experimentally observed surface melting temperature of a 38 nm gold nanoparticle, which is smaller than the particles we consider, was found to be  $\sim 1067 \text{ K}$ .<sup>40</sup> Additional experiments performed on gold nanoparticles show significant surface melting effects can occur even at lower temperatures, given a sufficiently long period of time (timescales ranging from hours to days). As an example, nanorods of various lengths can be converted into spheres at 523 K in 60 min.<sup>41</sup> In order to avoid

high temperature damage to the particle, the laser power level and pulse duration must be carefully chosen, with special attention given to laser heating immediately after bubble nucleation while the nanoparticle is essentially insulated. We use modelling to carefully select the laser pulse duration so as to constrain the heating to keep the nanoparticle below a maximum temperature of 1100 K. The modelling enables rapid parametric screening to achieve this goal.

## 2.4 Simulated nanostructures

We apply the theory to three different gold nanostructures: spheres, rods and tori. The LSPR wavelengths for these geometries are quite different.<sup>3</sup> Gold nanospheres have an absorption peak that occurs at an LSPR wavelength of approximately 530 nm, depending on the background medium. This resonance is independent of the field polarization because of spherical symmetry. In contrast, nanorods have more complex absorption spectra that depend on both their aspect ratio (length/width) and their orientation relative to the polarization of the incident light. A longer resonant wavelength occurs when the polarization is aligned along the length of the nanorod (longitudinal resonance) as compared to when it is aligned transverse (orthogonal) to the length. Nanorods can be designed and synthesized so that the longitudinal resonance is in the NIR. This is especially useful for bioapplications because light has its maximum depth of penetration in tissue in the NIR window, also referred to as the biological optical window (*e.g.* 650–900 nm). Thus, more efficient and effective photothermal therapy can be realized when the plasmon resonance is tuned to the NIR. Nanotori also have complex absorption spectra, but these are less well studied than nanospheres and nanorods. The absorption spectra depends on the ratio of their major to minor radii as well as their orientation relative to the polarization of the incident light. A longer resonant wavelength occurs when the incident field is polarized perpendicular to the axis of rotation as compared to when it is polarized parallel to this axis. Nanotori can be dispersed in fluid<sup>42</sup> and synthesized with their LSPR resonance in the NIR, which makes them useful for photothermal therapy.

## 3. Spherical nanoparticles

We first consider bubble nucleation around a gold nanosphere (Fig. 1 and 2). A photonic analysis is performed to quantify photothermal energy conversion within the sphere. The power absorbed by the sphere  $Q_{abs}(\lambda)$  is computed as a function wavelength at a nominal irradiance with TEM field polarization. The wavelength that produces the highest absorption is identified as the plasmon resonant wavelength. Once the photonic analysis is complete, a CFD analysis is performed to determine a power level for heat generation within the nanosphere and a corresponding pulse duration that are sufficient to create bubble nucleation without irreversible damage to the particle, *i.e.* keeping its peak temperature below its melting or even vaporization temperature. Once the viable power level and pulse duration are known, the laser irradiance needed to generate this power is back-calculated from the results of the photonic analysis.

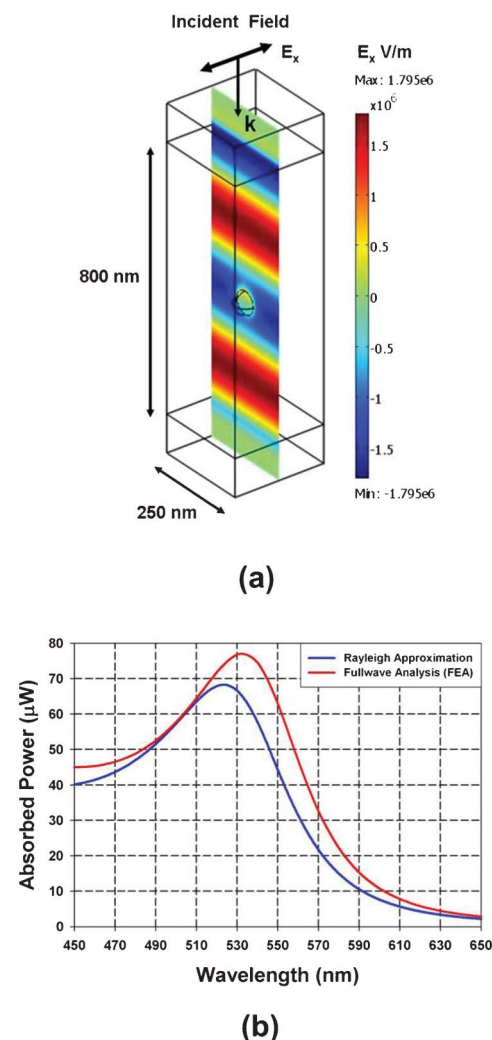


Fig. 2 Photonic analysis of the nanosphere: (a) computational domain and field analysis, (b) absorbed power vs. wavelength.

### 3.1 Photonic analysis

For analysis purposes, we have chosen a nanosphere with a diameter of 60 nm. The computational domain spans 1000 nm in the direction of propagation ( $z$ -axis), and 250 nm in both the  $x$  and  $y$  directions. The nanosphere is centred at the origin (Fig. 2a). The PMLs at the top and bottom of the computational domain are 100 nm in height. This leaves 800 nm of physical domain along the  $z$ -axis. PEC boundary conditions are applied at the boundaries perpendicular to the  $E$  field at  $x = \pm 125$  nm, and PMC boundary conditions are applied at the boundaries perpendicular to the  $H$  field at  $y = \pm 125$  nm. These conditions mimic a 2D array of identical nanospheres with a centre-to-centre lattice spacing of 250 nm in both the  $x$  and  $y$  directions. The sphere is illuminated with a downward directed uniform TEM plane wave with the  $E$  parallel to the  $x$ -axis. The incident field is generated by a time-harmonic surface current (not shown) positioned in the  $x$ - $y$  plane 400 nm above the centre of the nanosphere, *i.e.* immediately below the upper PML as described in the references.<sup>37,38</sup> We use a cubic vector finite element formulation with a total of 29,615 tetrahedral elements in the computational domain. The time-averaged power absorbed by

the nanosphere was computed for a range of wavelengths that spanned 450 nm to 650 nm in 2 nm increments. All the photonic analysis in this study was performed on a standalone modern workstation and the analysis of each geometry took several hours to complete.

The irradiance of the incident laser light is given by:

$$I_{inc} = \frac{c\epsilon_0 n_{H_2O}}{2} |E_{inc}|^2 \quad (10)$$

Throughout this analysis  $E_{inc} = 2 \times 10^6 \text{ V m}^{-1}$  and therefore the nominal irradiance for all of our simulations is  $I_{inc} = 7 \text{ mW } \mu\text{m}^{-2}$ .

We computed the absorbed power using both the numerical model and an analytical analysis, which is based on Rayleigh scattering theory<sup>43</sup>

$$Q_{abs} = k \text{Im}g(\alpha) I_{inc} \quad (11)$$

where  $k = 2\pi n_{H_2O}/\lambda$  and  $\alpha$  is the complex-valued polarizability of the sphere.

$$\alpha = \frac{4\pi\alpha_0\epsilon_0}{\left[1 - \alpha_0 \left(\frac{k^2}{a} - \frac{2}{3}ik^3\right)\right]} \quad (12)$$

where  $\alpha_0 = R_p^3(\epsilon_r - 1)/(\epsilon_r + 2)$  and  $R_p$  and  $\epsilon_r$  are the radius and relative permittivity of the sphere, respectively.<sup>37</sup> The plasmon resonance wavelength was found to be 532 nm based on the numerical analysis and the corresponding power absorbed by the nanosphere is 76  $\mu\text{W}$  (with  $I_{inc} = 7 \text{ mW } \mu\text{m}^{-2}$ ) as shown in Fig. 2b. The analytical analysis is also plotted and it yields a somewhat lower and narrower absorption profile because it is based on a dipole approximation, whereas the numerical model takes into account absorption and scattering due to higher order multipole terms. We use the results of the photonic analysis to determine the laser irradiance needed to effect bubble nucleation, which is based on fluidic analysis as described in the following.

### 3.2 Fluidic analysis

A CFD analysis was performed to determine viable power levels and pulse durations that produce bubble nucleation with sustained bubble dynamics, without damaging the nanosphere. We chose such values that limit the maximum particle temperature to less than 1100 K. An axisymmetric CFD model was developed to model one quadrant of a gold sphere. The computational domain spanned 7 radii of the sphere (210 nm), with 1 nm cell widths in both the radial ( $r$ ) and axial ( $z$ ) direction. Symmetry boundary conditions were imposed along both the  $r$ - and  $z$ -axes. The former accounted for the lower half of the sphere, while the latter accounted for its axial symmetry. The pressure and temperature throughout the computational domain were initialized to 1 Atm ( $1 \times 10^5 \text{ N m}^{-2}$ ) and  $T = 300 \text{ K}$ , respectively. A stagnation pressure condition ( $1 \times 10^5 \text{ N m}^{-2}$ ) was imposed at the outer  $r$  and  $z$  boundaries along with a Dirichlet condition set to the ambient temperature,  $T = 300 \text{ K}$ . These initial and boundary conditions were used for all the fluidic analysis.

A preliminary CFD thermal analysis (without phase change) was performed to determine power levels and pulse durations

that increase the temperature of the sphere from its initial ambient value ( $T = 300 \text{ K}$ ) to the supercritical temperature of 580 K. We computed the temperature of the nanosphere during heating for a range of power levels and pulse durations. The latter was chosen to be from 2 to 5 ns so as to exceed the non-equilibrium time constants of the photothermal process as described above. The CFD analysis was guided by analytical formulas for heat transfer as appropriate. This preliminary analysis was performed because it is far less computationally intensive than the full phase change and bubble nucleation analysis, while at the same time providing an intuitive understanding of thermal diffusion from the sphere to the fluid up to nucleation.

Once the preliminary thermal calculations were complete, CFD simulations of bubble nucleation were performed using power levels selected from the preliminary analysis, but with longer pulse durations to ensure nucleation and sustained bubble dynamics. For the sphere, we concluded that an adequate power for nucleation without melting was 152  $\mu\text{W}$ , with a pulse duration of 5 ns. Given these values, and the results from the photonic analysis (Fig. 2a), we determined that a laser operating at  $\lambda = 532 \text{ nm}$  with an irradiance of  $I_{inc} = 14 \text{ mW } \mu\text{m}^{-2}$  is sufficient to generate a bubble under controlled conditions, *i.e.* without melting the sphere. The fluidic analysis at this power and pulse duration is shown in Fig. 3. This plot shows the temperature of the nanosphere during and after the heat pulse. Various portions of the plot are labelled from (a)–(e) and there are corresponding images of the nanosphere and bubble at these times that show the generation and collapse of a primary and secondary bubble.

Initially the nanosphere and the domain are at a temperature of 300 K. After 0.2 ns the particle is illuminated and starts to heat. During the first 3.8 ns of heating, the temperature of the sphere gradually increases (Fig. 3a) from the ambient 300 K to the superheat temperature 580 K at which point a bubble is nucleated around it. Once this occurs, the sphere is surrounded by vapour and the heat transfer from its surface is greatly reduced. Thus, its temperature increases rapidly as it is still absorbing energy from the incident light. The particle reaches a peak temperature of approximately 1080 K, which occurs at the end of the heat pulse (5ns), while it is surrounded by vapour (Fig. 3b).

Once the bubble has nucleated, which occurs just after 4 ns, it expands due to its high pressure relative to the surrounding fluid, which is initially at 1 Atm. The bubble reaches its maximum volume 5.4 ns after the heating starts. At its largest extent, the bubble is characterized by a slightly elliptical shape, which is due to small numerical variations in the initial nucleation and growth of the bubble at the surface of the particle. The maximum size is approximately 50 nm and 60 nm in the  $r$  and  $z$  directions, respectively. Subsequently, 7 ns after the onset of heating, the bubble collapses, bringing fluid back in contact with the particle, which cools it from its peak temperature of 1080 K to approximately 960 K (Fig. 3c). As the particle cools, the fluid temperature increases until it reaches the superheat temperature once again, at which point a secondary bubble is generated (Fig. 3d). The secondary bubble reaches its maximum size 8.2 ns after the initial onset of heating. At this point, the bubble is characterized by a spherical shape and its maximum size is

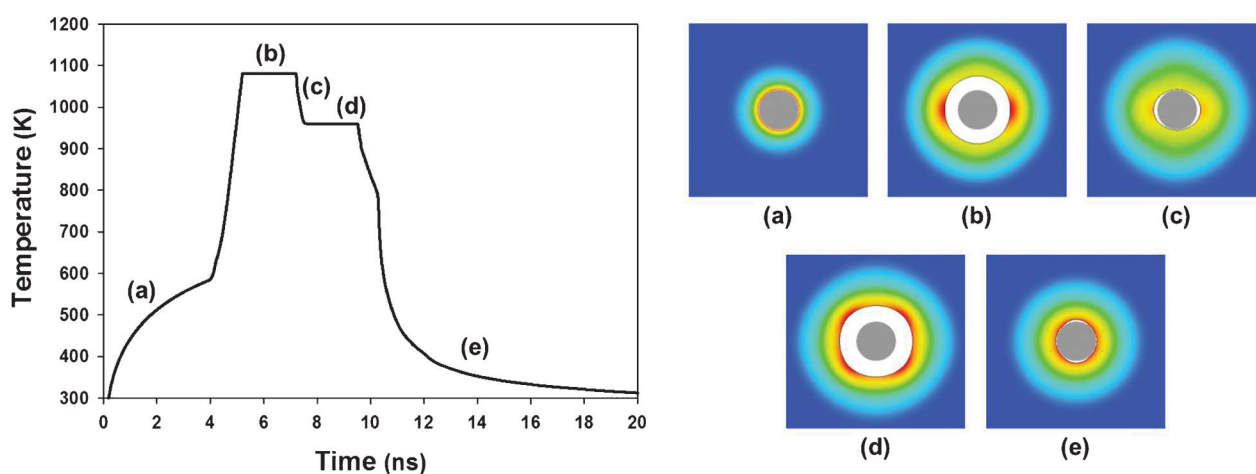


**Fig. 3** Photothermal heat cycle of the nanosphere (cross-sectional view): (a) initial heating, (b) primary bubble, (c) primary bubble collapse, (d) secondary bubble, (e) secondary bubble collapse with cooling.

approximately 50 nm in radius. Eventually, the second bubble collapses bringing fluid in contact with the sphere once again, and the sphere cools it towards the ambient temperature (Fig. 3e). It is important to note that the number of bubble cycles generated and the dynamics during each cycle can in principle be controlled by tuning the power and duration of the heat pulse. Finally, the fluidic analysis for each particle can take up to 24 h of run time on a standalone workstation.

#### 4. Nanorods

Next, we studied the use of gold nanorods for bubble nucleation. These structures have plasmonic properties that are different than their spherical counterparts. Most notably, they have two distinct plasmon resonant frequencies, one higher and one lower, corresponding to transverse and longitudinal polarization modes, respectively. The higher frequency (shorter wavelength) occurs when the field is polarized transverse to the rod (*i.e.* perpendicular to the major axis) and is similar to that of a spherical particle. The lower frequency (longer wavelength) depends on the aspect ratio of the nanorod and can be tuned through synthesis for specific applications. The ability to tune the resonance in this fashion has spawned a growing interest in the use of gold nanorods, especially for bioapplications that require plasmon resonance tuned to NIR wavelengths to achieve deeper and more effective penetration of light into a target tissue. Gold nanorods have additional interesting plasmonic features, notably, a narrower plasmon bandwidth<sup>14</sup> and greater field enhancement than spherical particles at comparable resonance frequencies and volumes.

##### 4.1 Photonic analysis

We modelled the nanorod as a cylinder with hemispherical caps. For this analysis, we chose the length and diameter of the nanorod to be 60 nm and 17 nm, respectively. The computational domain for the photonic analysis spans 110 nm in the direction of propagation ( $z$ -axis), and 150 nm in both the  $x$  and  $y$  directions as shown in Fig. 4a. The nanorod is centred at the origin with its length aligned with the  $x$ -axis. As before, there are PMLs at the top and bottom of the computational domain,

which are 25 nm in height. This leaves 60 nm of physical domain along the  $z$ -axis. PEC boundary conditions are applied at boundaries perpendicular to the  $E$  field at  $x = \pm 75$  nm and PMC boundary conditions are applied at boundaries perpendicular

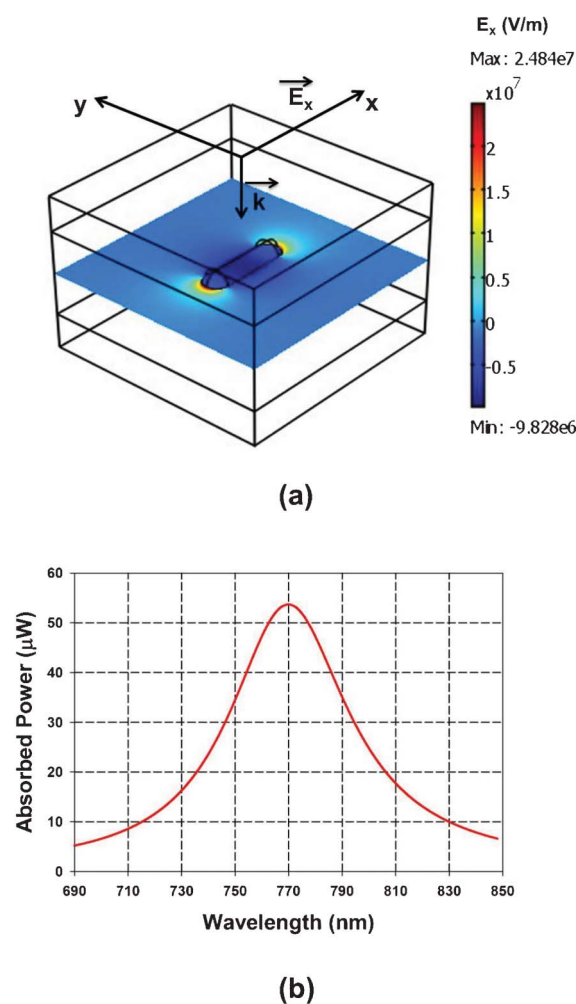


**Fig. 4** Photonic analysis of the nanorod: (a) computational domain and field analysis, (b) absorbed power vs. wavelength.

to the H field at  $y = \pm 75$  nm. These conditions mimic a 2D array of identical nanorods with a centre-to-centre lattice spacing of 150 nm in both the  $x$  and  $y$  directions. The nanorod is illuminated with a downward directed uniform TEM plane wave with  $\mathbf{E}$  aligned along the length of the nanorod, *i.e.* parallel to the  $x$ -axis. As in the previous analysis, the incident field is generated by a time-harmonic surface current positioned in the  $x$ - $y$  plane immediately below the upper PML. Cubic vector finite elements were used and there were a total of 41,932 tetrahedral elements in the computational domain. The time-averaged power absorbed by the nanorod was computed for wavelengths that spanned 600 nm to 900 nm in 2 nm increments. The plasmon resonance wavelength was found to be 770 nm and the corresponding power absorbed is  $53.7 \mu\text{W}$  (with  $I_{inc} = 7 \text{ mW } \mu\text{m}^{-2}$ ) as shown in Fig. 4b.

#### 4.2 Fluidic analysis

A CFD analysis was performed to determine a power level and pulse duration that would produce bubble nucleation and sustained dynamics without melting the nanorod. An axisymmetric CFD model was used for the analysis. The computational domain spanned 150 nm in both the  $r$  and  $z$  directions. A uniform mesh of 0.5 nm cells in both directions was used. Symmetry boundary conditions were imposed along both the  $r$  and  $z$  axes. The former accounted for the lower half of the nanorod while the latter accounted for its axial symmetry. The same initial and boundary conditions were used as in the case of the nanosphere. However, it should be noted that unlike a sphere, a nanorod is characterized by different heat transfer coefficients along the surface of its cylindrical portion as compared to its spherical tips. Thus, bubble nucleation and growth can evolve differently over these surfaces.

As in the case of the sphere, a preliminary CFD analysis (without phase change) was performed to determine a range of power levels and pulse durations that increase the temperature of the nanorod from ambient to the supercritical temperature. Based on this analysis, we identified viable power levels and pulse durations limited to a range of 1.5 to 3 ns. We then used this data in a parametric CFD analysis that accounted for bubble nucleation, only with slightly extended pulse durations so as to

ensure a sustained bubble without damaging the particle. It was found that an adequate power for nucleation without melting the nanorod was  $76.8 \mu\text{W}$ , with a pulse duration of 1.9 ns. Given these values and the results of the photonic analysis (Fig. 4b), we determined that a laser operating at  $\lambda = 770$  nm with an irradiance of  $I_{inc} = 10 \text{ mW } \mu\text{m}^{-2}$  is sufficient to generate and sustain a bubble without melting the nanorod. The photothermal process at this power and pulse duration is shown in Fig. 5. This figure shows the temperature of the nanorod during and after the heat pulse along with corresponding images that show the generation and collapse of the nanobubble.

Initially, the nanorod is at ambient temperature of 300 K. After 0.2 ns the nanorod is illuminated and its temperature starts to increase. During the first 1.7 ns of heating, the temperature of the nanorod gradually increases to the superheat temperature (Fig. 5a), at which point a bubble is nucleated around its tips. Once this occurs the particle is partly surrounded by vapour and heat transfer from its surface is greatly reduced. Its temperature increases rapidly at this point as it is still absorbing energy from the incident light. The nanorod reaches a maximum instantaneous temperature of 915 K, which occurs at the end of the heat pulse (1.9 ns in duration) when it is still surrounded, in part, by liquid (Fig. 5b). The remaining liquid completely evaporates by approximately 2.7 ns after the onset of heating, and in doing so, the nanorod cools from its peak temperature to approximately 765 K.

As soon as the bubble has nucleated, it expands due to its high pressure relative to the surrounding fluid. It reaches its maximum size 3 ns after the onset of heating at which point it has an elliptical shape and it has dimensions of approximately 45 nm and 65 nm in the  $r$  and  $z$  directions, respectively. Eventually, at 4.4 ns the nanobubble collapses, bringing fluid back in contact with the tips of the nanorod (Fig. 5d) and starts cooling it. The nanorod is then further cooled to ambient temperature when the rest of the fluid comes in contact with it, 5.2 ns after the onset of heating (Fig. 5e).

#### 5. Torus

The last geometry we study is the nanotorus. Gold nanotori have a complex multimodal plasmonic response. For incident light

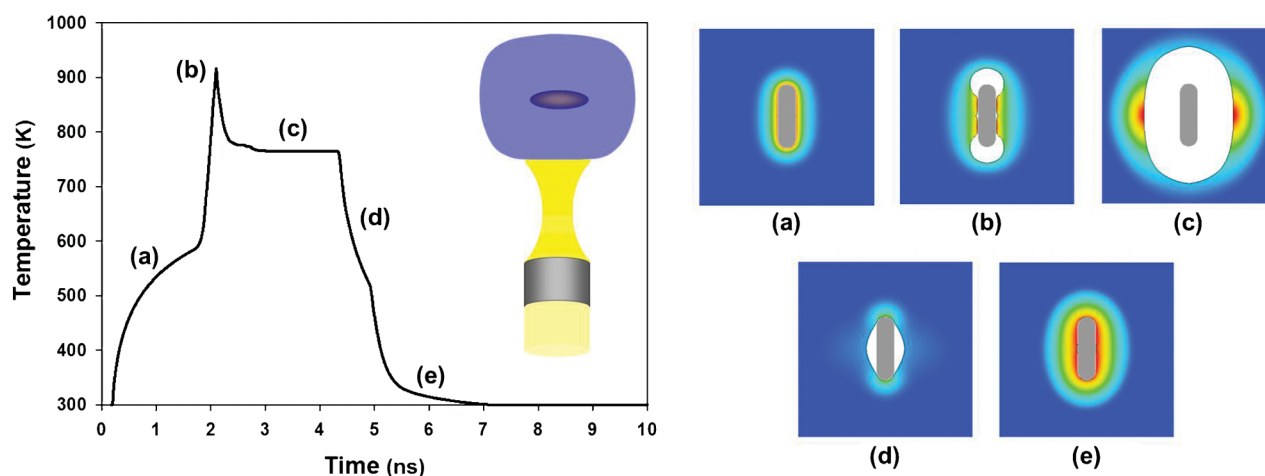


**Fig. 5** Photothermal heat cycle of the nanorod (cross-sectional view): (a) initial heating, (b) bubble formation, (c) bubble (maximum size), (d) bubble collapse, (e) cooling.

polarized in the plane of the torus, the optical spectrum is characterized by a long wavelength resonance, and a short wavelength resonance that corresponds to excitation of higher order modes. We are most interested in the long wavelength resonance as it can be tuned by varying the major ( $R$ ) and minor ( $r$ ) radii of the torus, during synthesis.<sup>44,45</sup> Though nanorods also possess this feature, their longer (*e.g.* NIR) resonant wavelength will only be effective when the field is polarized along the major axis, which can be difficult to achieve in practice. However, given the symmetry of the torus, resonance can be achieved with the field polarization at any angle as long as it is in the plane of the torus. Thus, nanotori hold promise for more readily realized and efficient photothermal heating than nanorods, especially for bioapplications that require NIR illumination for maximum tissue penetration. In the following we consider a specific torus geometry with major and minor radii of  $R = 30$  nm and  $r = 10$  nm, respectively.

### 5.1 Photonic analysis

The computational domain for the torus spans 230 nm in the direction of propagation ( $z$ -axis), and 150 nm in both the  $x$  and  $y$  directions (Fig. 6a). The torus is centred at the origin and as above, there are PMLs at the top and bottom of the

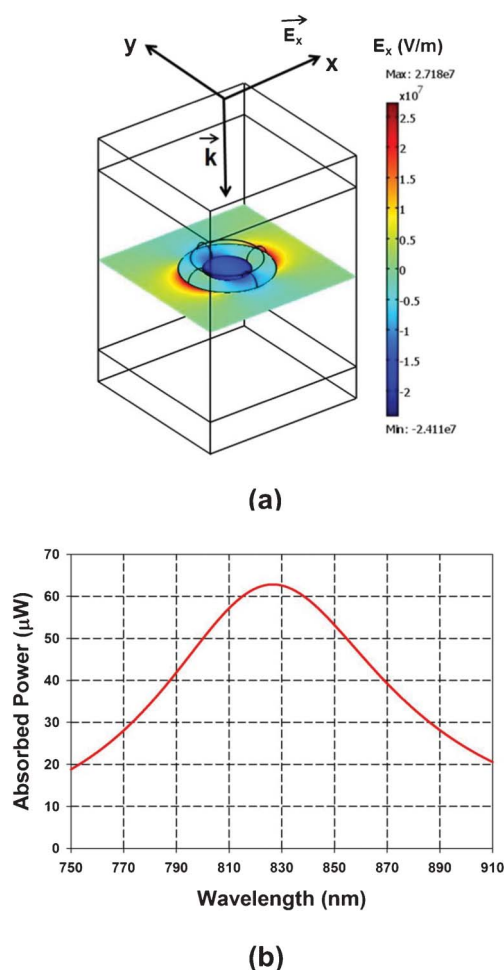


**Fig. 6** Photonic analysis of the nanotorus: (a) computational domain and field analysis, (b) absorbed power vs. wavelength.

computational domain, which are 30 nm in height. This leaves 170 nm of physical domain along the  $z$ -axis. Once again, PEC boundary conditions are applied at boundaries perpendicular to the  $\mathbf{E}$  field at  $x = \pm 75$  nm, and PMC boundary conditions are applied at boundaries perpendicular to the  $\mathbf{H}$  field at  $y = \pm 75$  nm. These conditions mimic a 2D array of identical nanotori with a centre-to-centre lattice spacing of 150 nm in both the  $x$  and  $y$  directions. The torus is illuminated with a downward directed uniform TEM plane wave with  $\mathbf{E}$  parallel to the  $x$ -axis (Fig. 6a). The incident field is generated by a time-harmonic surface current positioned in the  $x$ - $y$  plane 85 nm above the centre of the torus, *i.e.* directly below the upper PML. We performed a parametric analysis of the power absorbed by the torus as a function of wavelength for  $\lambda = 750$ –950 nm in 2 nm increments. As in the previous cases, cubic vector finite elements were used, in this case there were 28,668 tetrahedral elements in the computational domain. Plasmon resonance was found to occur at 828 nm and the corresponding power absorbed is 62.8  $\mu\text{W}$  (with  $I_{inc} = 7$  mW  $\mu\text{m}^{-2}$ ) as shown in Fig. 6b.

### 5.2 Fluidic analysis

CFD analysis was performed to determine the power and pulse duration required to achieve bubble nucleation without melting the torus. An axisymmetric model was used with a computational domain that spanned 200 nm in both the  $r$  and  $z$  directions. A uniform mesh of 1 nm cells in both dimensions was used. Symmetry boundary conditions were imposed along both the  $r$ - and  $z$ -axes. The former accounted for the lower half of the torus while the latter accounted for its axial symmetry. The initial and boundary conditions are the same as for the nanosphere.

As in the other cases, a preliminary thermal analysis (without phase change) was performed to determine power levels and pulse durations that increase the temperature of the torus from ambient to the supercritical temperature. We calculated the temperature of the torus during heating for a range of power levels and pulse durations. The latter was chosen to be from 2 to 5 ns. Once this analysis was complete, the results were used in a second parametric CFD analysis that included bubble nucleation to determine viable power levels and pulse durations that are sufficient to nucleate a sustained bubble without destroying the torus. It was found that an adequate power for nucleation was 172.8  $\mu\text{W}$ , with a pulse duration of 4.1 ns. Given these values and the results of the photonic analysis (Fig. 6b) we determined that a laser operating at the plasmon resonant wavelength of  $\lambda = 828$  nm with an irradiance of  $I_{inc} = 19.27$  mW  $\mu\text{m}^{-2}$  is sufficient to generate and sustain a bubble without melting the torus. The fluidic analysis at this power and pulse duration is shown in Fig. 7. This plot shows the temperature of the torus throughout the photothermal process along with corresponding images of the bubble dynamics.

Initially the torus is at ambient temperature. After 0.2 ns it is illuminated and its temperature begins to rise. During the first 3.4 ns of heating, its temperature gradually increases (Fig. 7a) to the superheat temperature, at which point a bubble is nucleated around it. Once this occurs the torus is surrounded by vapour and its temperature increases rapidly as it is still absorbing energy. It reaches a peak temperature of approximately 1000 K,

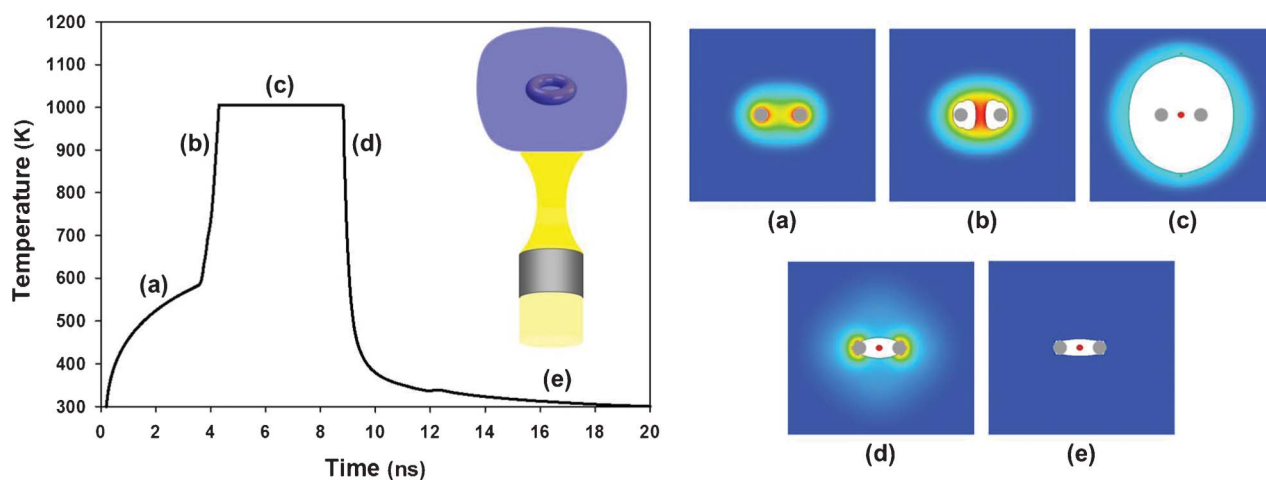


**Fig. 7** Photothermal heat cycle of the nanotorus (cross-sectional view): (a) initial heating, (b) bubble formation, (c) bubble (maximum size), (d) bubble collapse, (e) cooling

which occurs at the end of the heat pulse (4.1 ns), at which point it is completely surrounded by vapour (Fig. 7b).

As soon as the bubble has nucleated, it expands and reaches its maximum size at 5.4 ns after the onset of heating. At this time the bubble has a spherical shape, approximately 80 nm in radius. An interesting feature of this process is the residue of an isolated drop of heated fluid that forms in the middle of the torus during the bubble expansion as seen in Fig. 7c. Eventually, 8.7 ns after the onset of heating, the nanobubble collapses, bringing fluid back in contact with the torus (Fig. 7d). Consequently, it slowly cools to the ambient temperature as more of the fluid comes in contact with it (Fig. 7e). It is instructive to note that the capillary force that acts to collapse the bubble is relatively weak because of the relatively large radius of curvature that defines the fluid–vapour interface as it gets closer to the torus. Thus, the nanobubble requires a substantial amount of time to completely collapse, compared to other geometries.

## 6. Multiple nanorods

We performed thermal simulations of a multi-nanorod system to examine effects of cooperative heating. We studied an evenly spaced 3-dimensional array of nanorods that are 60 nm in length and 17 nm in diameter, *i.e.* identical to the single nanorod system. We systematically varied the surface-to-surface spacing between the nanorods from 1 to 7 radii, in both  $r$  and  $z$  directions. We used 3-D CFD analysis (without phase change) with a computational domain that spanned from 12.75 nm to 38.25 nm in both  $x$  and  $y$  directions and from 34.25 nm to 59.75 nm in the  $z$  direction, depending on the distance between the nanorods. Using the same amount of power in each nanorod as in the single nanorod case, we calculated the pulse duration that is required to heat the nanorods to the superheat temperature. The results of this parametric analysis are presented in Fig. 8. Based on our calculations, it can be concluded that for a distance of 1 radius between the nanorods, only 39% of the energy is required to reach the nucleation temperature as compared to the single nanorod system. Moreover, all cooperative heating effects become negligible after a distance of 7 radii in all directions.

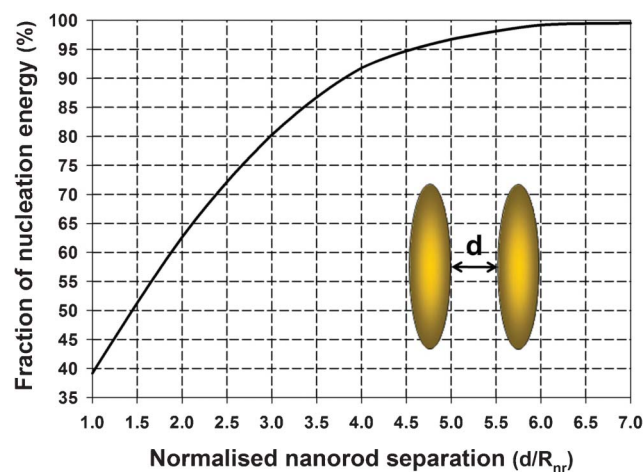


**Fig. 8** Percentage of single nanorod energy required to achieve multi-rod nucleation vs. nanorod separation.

## 7. Multiple tori

We also studied a coaxial multi-tori system comprised of 2 identical tori with the same dimensions as in the single torus analysis, *i.e.* major and minor radii of  $R = 30$  nm and  $r = 10$  nm, respectively. We demonstrate that this 2 tori system has distinct advantages over a single torus system; notably, significant cooperative heating that results in larger nanobubbles with less energy.

### 7.1 Thermal analysis

A parametric thermal analysis was performed to examine the cooperative heating effects of the 2-tori system. Using the same amount of power ( $172.8 \mu\text{W}$ ) as in the single torus case, we calculated the pulse duration required for the temperature of the tori to reach the superheat temperature. This analysis was performed for a range of torus-to-torus spacing spanning 1 to 10 minor radii between the edges of the tori (*i.e.* 10 to 100 nm). We used an axisymmetric model with a computational domain that spanned 200 nm and 200–245 nm in the  $r$  and  $z$  directions,

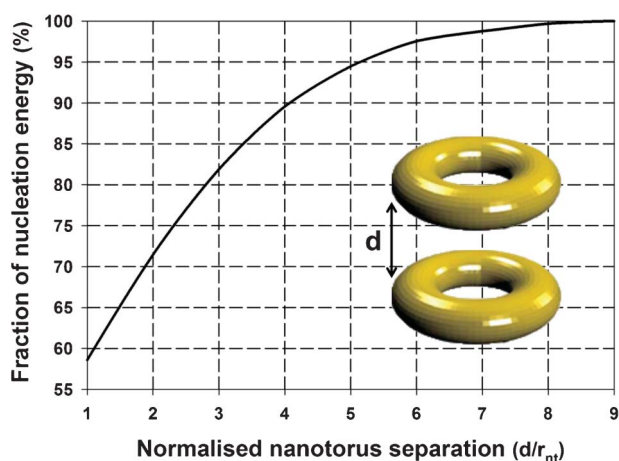


**Fig. 9** Percentage of single nanotorus energy required to achieve 2 torii nucleation vs. nanotorus separation.

respectively (depending on the distance between the torii). The results of this analysis are presented in Fig. 9. Note, for example, that for a distance of 1 radius between the torii, the energy required to achieve the superheat temperature is only 58% of that of the single torus system. In addition, all cooperative heating effects become negligible after a separation distance of 9 radii.

## 7.2 Cooperative bubble nucleation

We studied bubble nucleation for the 2 torii system. The distance between the centres of the torii was set to 60 nm (*i.e.* 4 minor radii spacing, edge-to-edge). We used an axisymmetric model in which the computational domain spanned 200 nm and 215 nm in the  $r$  and  $z$  directions, respectively, with a 1 nm cell size in both directions. Symmetry boundary conditions were imposed along both the  $r$ - and  $z$ -axes. The former accounted for the second torus while the latter accounted for their axial symmetry. The same initial and boundary values as in the single torus case were applied. We first determined a range of viable power levels and pulse durations and then used this data in a parametric CFD phase change analysis to select a power level and pulse duration that are sufficient to generate a bubble without damaging the torii. It was found that respective values of 72.8  $\mu\text{W}$  and 3.45 ns

would serve this purpose. The fluidic analysis at this power and pulse duration is shown in Fig. 10. This plot shows the temperature of the torii and corresponding images that show the generation and collapse of combined nanobubbles.

Initially, the torii are at ambient temperature and after 0.2 ns they are illuminated. During the first 2.9 ns of heating, their temperature gradually increases to the superheat temperature, at which point, separate bubbles start to nucleate around the torii (Fig. 10a). It should be noted that this heating process requires 10% less energy than the single torus system, due to cooperative heating between the torii, as shown in Fig. 9. Once the torii are partly surrounded by vapour, the heat transfer from their surface is negligible and their temperature increases rapidly as they continue to absorb energy. The torii reach an instantaneous peak temperature of approximately 790 K, which occurs at the end of the heat pulse (3.45 ns) at which point they are partially surrounded by liquid (Fig. 10b). This remaining liquid completely evaporates at approximately 4.2 ns after the onset of heating, and during evaporation the torii cool from their peak temperature to 740 K.

As soon as the bubbles have nucleated, they expand and as they do so, isolated drops of hot fluid form within the bubble close to the torii, similar to what was observed in the single torus system. The bubbles eventually merge and continue to grow as a single bubble, which reaches its maximum size 6.3 ns after the onset of heating. At its largest extent, the bubble has an elliptical shape of approximately 95 nm and 150 nm in the  $r$  and  $z$  directions, respectively (Fig. 10c). Eventually, 10 ns after onset of heating, the nanobubble collapses bringing fluid back in contact with the torii. A minor bubble forms in the space between the torii and shrinks slowly due to a relatively weak capillary force (Fig. 10d). The torii are then further cooled to ambient temperature and the bubble shown in Fig. 10d transforms into 2 smaller bubbles (Fig. 10e). It should also be noted that, due to relatively weak capillary forces (corresponding to a large radius of curvature at the liquid–vapour interface) the nanobubbles shown in Fig. 10e require a substantial amount of time to completely collapse. As with all systems studied, the number of bubbles generated and their dynamics can be controlled by tuning the power level and duration of the heat pulse. In conclusion, the 2 coaxial torii system was able to generate a bubble approximately 3.6 times larger than in the single torus

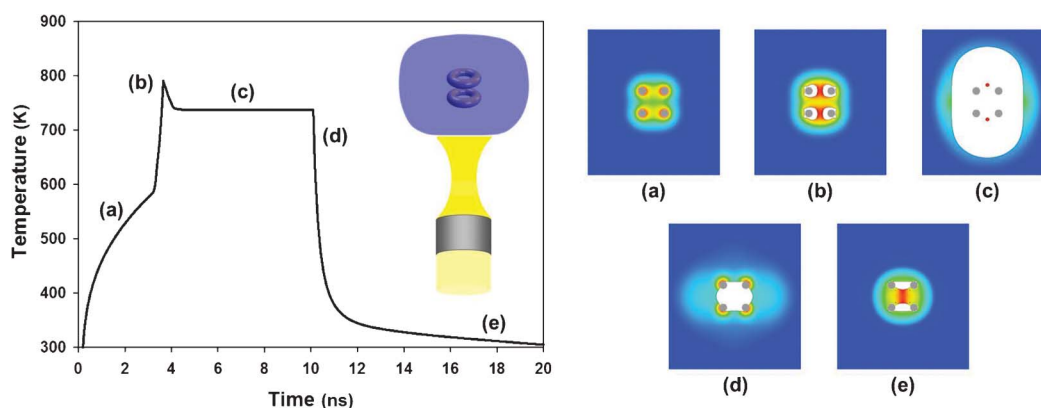


**Fig. 10** Photothermal heat cycle of a 2 nanotorii system (cross-sectional view): (a) initial heating, (b) bubble formation, (c) bubble (maximum size), (d) bubble collapse, (e) further bubble collapse and cooling.

case while requiring less than 85% of the energy consumed by the single torus system.

## 8. Discussion

The modelling approach presented above can be used for the rational design of pulsed-laser plasmon-assisted photothermal applications. The first step is to identify a range of viable operating wavelengths (spectral window) for the particular application. Next, candidate nanostructures are designed using photonic analysis, *i.e.* geometric parameters (*e.g.* length, width, radii *etc.*) are determined that render LSPR wavelengths within the desired spectral window. The absorption spectra for the different candidate nanostructures are computed in order to determine the power they absorb as a function of the incident field polarization and irradiance. Once a viable nanostructure has been identified, a CFD-based thermal analysis (without bubble nucleation) is performed to determine the laser pulse duration and power absorption needed to raise the particle temperature to the superheat temperature of the surrounding fluid in order to achieve bubble nucleation. The pulse duration should be chosen to be multiple nanoseconds in order to justify the application of continuum theory as described above. Once the absorption spectra and required power level have been determined for a given nanostructure, the incident laser intensity needed for bubble nucleation can be back calculated. Finally, a CFD-based thermal-fluidic-phase change analysis is performed of the heated nanoparticle in fluid in order to study the dynamics of the generated bubble and its effect on the surrounding fluid.

It should be noted that this approach applies to an isolated nanoparticle or a highly ordered collection of nanoparticles (*e.g.* a pair of coaxial tori) in fluid. However, in general, there can be a large number of particles (dispersion) with a random distribution of orientations. In this case, an average absorption can be calculated and bubble generation can be studied as above, assuming that the particles are non-interacting.

## 9. Conclusions

Applications of nanoscale photothermal phenomena involving pulsed laser illuminated metallic nanoparticles are growing rapidly across various and diverse emerging fields. The use of plasmonics for such applications has many advantages. It enables remote, all optical activation *via* laser illumination, efficient energy conversion at plasmon resonance over tunable wavelengths that span the UV to NIR spectrum and nanoscale spatial resolution with temporal probing down to ultra-fast time frames.

In this paper we have for the first time used combined continuum level computational electromagnetic and fluid dynamic analysis to study nanosecond-pulsed laser heating and bubble generation due to subwavelength gold nanospheres, nanorods and nanotori. We have used the modelling to determine power levels and pulse durations that are sufficient to generate a desired bubble size and dynamics, while avoiding damage to the particle through excessive heating. We have also used modelling to quantify the effects cooperative heating in multiparticle systems. We have demonstrated for the first time that more robust bubble generation can be achieved with lower

laser energy when particles are within a few radii of one another as compared to corresponding single particle systems. The modelling approach presented here enables fundamental understanding of plasmon-assisted photothermal heating including fluidic phase change leading bubble nucleation. It should prove useful for the rational design of novel nanoparticle-based photothermal systems.

## Acknowledgements

The authors would like to thank Melissa Carter, Dr James M. Brethour and Tony Hirt of Flowscience Corp. for numerous valuable technical discussions.

## References

- 1 G. Frens, *Nature Phys. Sci.*, 1973, **241**, 20.
- 2 S. L. Goodman, G. M. Hodges and D. C. Livingston, *Scanning Electron Microsc.*, 1980, **2**, 133–146.
- 3 P. K. Jain, X. H. Huang, I. H. El-Sayed and M. A. El-Sayed, *Acc. Chem. Res.*, 2008, **41**, 1578–1586.
- 4 U. Kreibig and M. Vollmer, *Optical Properties of Metal Clusters*, Springer, Berlin, 1995.
- 5 N. Lewinski, V. Colvin and R. Drezek, *Small*, 2008, **4**, 26–49.
- 6 S. Schultz, D. R. Smith, J. J. Mock and D. A. Scultz, *Proc. Natl. Acad. Sci. U. S. A.*, 2000, **97**, 996–1001.
- 7 A. L. Oldenburg, M. N. Hansen, D. A. Zweifel, A. Wei and S. A. Boppart, *Opt. Express*, 2006, **14**, 6724–6738.
- 8 A. Agarwal, S. W. Huang, M. O'Donnel, K. C. Day and M. Day, *J. Appl. Phys.*, 2007, **102**, 064701.
- 9 H. Wang, T. B. Huff, D. A. Zweifel, W. He, P. S. Low, A. Wei and J. Cheng, *Proc. Natl. Acad. Sci. U. S. A.*, 2005, **102**, 15752–15756.
- 10 X. Huang, I. H. El-Sayed, W. Qian and M. A. El-Sayed, *J. Am. Chem. Soc.*, 2006, **128**, 2115–2120.
- 11 S. Hashimoto, D. Werner and T. Uwada, *J. Photochem. Photobiol., C*, 2012, **13**, 28–54.
- 12 O. Ekici, R. K. Harrison, N. J. Durr, D. S. Eversole, M. Lee and A. Ben-Yakar, *Journal of Physics D-Applied Physics*, 2008, 41.
- 13 E. Hao, G. Schatz and J. Hupp, *J. Fluoresc.*, 2004, **14**, 331–341.
- 14 C. Sonnichsen, T. Franzl, T. Wilk, G. von Plessen, J. Feldmann, O. Wilson and P. Mulvaney, *Phys. Rev. Lett.*, 2002, **88**, 077402.
- 15 E. Hao and G. Schatz, *J. Chem. Phys.*, 2004, **120**, 357–366.
- 16 E. Y. Lukianova-Hleb, E. Y. Hanna, J. H. Hafner and D. O. Lapotko, *Nanotechnology*, 2010, 21.
- 17 G. Huttmann, B. Radt, J. Serbin, B. I. Lange and R. Birngruber, *Med. Laser Appl.*, 2002, **17**, 9–14.
- 18 C. M. Pitsillides, E. K. Joe, X. Wei, R. R. Anderson and C. P. Lin, *Biophys. J.*, 2003, **84**, 4023–4032.
- 19 G. Huttmann, C. Yao and E. Endl, *Med. Laser Appl.*, 2005, **20**, 135–139.
- 20 R. R. Letfullin, C. Joenathan, T. F. Georger and V. P. Zharov, *Nanomedicine*, 2006, **1**, 473–480.
- 21 G. V. Hartland and M. Hu, *Proc. SPIE-Int. Soc. Opt. Eng.*, 2002, **4807**, 166–176.
- 22 G. V. Hartland, M. Hu and J. E. Sader, *J. Phys. Chem. B*, 2003, **107**, 7472–7278.
- 23 M. Hu and G. V. Hartland, *J. Phys. Chem. B*, 2002, **106**, 7029–7033.
- 24 A. N. Volkov, C. Sevilla and L. V. Zhigilei, *Appl. Surf. Sci.*, 2007, **253**, 6394–6399.
- 25 D. Lapotko, *Nanomedicine*, 2009, **4**, 813–845.
- 26 D. Lapotko, *Opt. Express*, 2009, **17**, 2538–2556.
- 27 D. Lapotko, *Int. J. Heat Mass Transfer*, 2009, **52**, 1540–1543.
- 28 D. Lapotko, E. Lukianova, M. Potapnev, O. Aleinikova and A. Oraevsky, *Cancer Lett.*, 2006, **239**, 36–45.
- 29 D. O. Lapotko, E. Lukianova and A. A. Oraevsky, *Lasers Surg. Med.*, 2006, **38**, 631–642.
- 30 E. Y. Lukianova-Hleb, A. Belyanin, S. Kashinath, X. Wu and D. O. Lapotko, *Biomaterials*, 2012, **33**, 1821–1826.
- 31 E. Y. Lukianova-Hleb, I. I. Koneva, A. O. Oginsky, S. La Francesca and D. O. Lapotko, *J. Surg. Res.*, 2011, **166**, e3–e13.

- 32 D. K. Roper, W. Ahn and M. Hoepfner, *J. Phys. Chem. C*, 2007, **111**, 3636–3641.
- 33 A. Pattamatta and C. K. Madnia, *Journal of Heat Transfer-Transactions of the Asme*, 2010, 132.
- 34 P. G. Etchegoin, E. C. Le Ru and M. Meyer, *Journal of Chemical Physics*, 2006, 125.
- 35 P. G. Etchegoin, E. C. Le Ru and M. Meyer, *Journal of Chemical Physics*, 2007, 127.
- 36 P. B. Johnson and R. W. Christy, *Phys. Rev. B: Solid State*, 1972, **6**, 4370–4379.
- 37 E. P. Furlani and A. Baev, *Physical Review E*, 2009, 79.
- 38 E. P. Furlani and A. Baev, *J. Mod. Opt.*, 2009, **56**, 523–529.
- 39 C. W. Hirt and B. D. Nichols, *J. Comput. Phys.*, 1981, **39**, 201–225.
- 40 S. Inasawa, M. Sugiyama and Y. Yamaguchi, *J. Phys. Chem. B*, 2005, **109**, 3104–3111.
- 41 H. Petrova, J. P. Juste, I. Pastoriza-Santos, G. V. Hartland, L. M. Liz-Marzan and P. Mulvaney, *Phys. Chem. Chem. Phys.*, 2006, **8**, 814–821.
- 42 C. K. Lee, H. Y. Tseng, C. Y. Lee, S. Y. Wu, T. T. Chi, K. M. Yang, H. Y. E. Chou, M. T. Tsai, J. Y. Wang, Y. W. Kiang, C. P. Chiang and C. C. Yang, *Biomed. Opt. Express*, 2010, **1**, 1060–1074.
- 43 H. C. van de Hulst, *Scattering of Light by Small Particles*, Dover Publications Inc, New York, 1981.
- 44 J. Aizpurua, P. Hanarp, D. S. Sutherland, M. Kall, G. W. Bryant and F. J. G. de Abajo, *Physical Review Letters*, 2003, 90.
- 45 C. M. Dutta, T. A. Ali, D. W. Brandl, T. H. Park and P. Nordlander, *Journal of Chemical Physics*, 2008, 129.